Inorganic Chemistry

Article

pubs.acs.org/IC

Lithium Storage Mechanisms and Effect of Partial Cobalt Substitution in Manganese Carbonate Electrodes

Shadi Mirhashemihaghighi,[†] Bernardo León,[†] Carlos Pérez Vicente,[†] José L. Tirado,*[,†] Radostina Stoyanova,[‡] Meglena Yoncheva,[‡] Ekaterina Zhecheva,[‡] Regino Sáez Puche,[§] Elena M. Arroyo,[§] and Julio Romero de Paz[§]

[†]Inorganic Chemistry Laboratory. Universidad de Córdoba. Edif. C3, Campus de Rabanales, 14071 Córdoba, Spain

[‡]Institute of General and Inorganic Chemistry, Bulgarian Academy of Sciences, Sofia, Bulgaria

[§]Inorganic Chemistry Laboratory, Universidad Complutense, Madrid, Spain

Supporting Information

ABSTRACT: A promising group of inorganic salts recently emerged for the negative electrode of advanced lithium-ion batteries. Manganese carbonate combines low weight and significant lithium storage properties. Electron paramagnetic resonance (EPR) and magnetic measurements are used to study the environment of manganese ions during cycling in lithium test cells. To observe reversible lithium storage into manganese carbonate, preparation by a reverse micelles method is used. The resulting nanostructuration favors a capacitive lithium storage mechanism in manganese carbonate with good rate performance. Partial substitution of cobalt by manganese improves cycling efficiency at high rates.

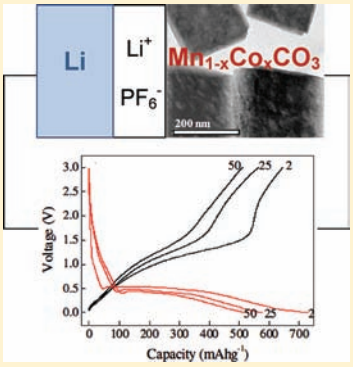

Active materials for the positive electrode of lithium-ion batteries were first found among lithium, transition-metal oxides with layered[1,2] and spinel-related[3,4] structures. Metal substitutions in these solids were found to have positive effects on electrode performance.[5,6] Besides, other pioneering works also showed that lithium, transition metal-oxysalts were particularly useful, with special emphasis on olivine-related phosphates.[7,8] In recent years an extended research activity has reached the silicate[9,10] and sulfate[11] families.

By analogy, active materials for the negative electrode of lithium-ion batteries involving conversion reactions were first found among binary transition metal oxides.[12,13] Further activity unfolded the positive effects of partial metal substitution in some of these materials.[14−16] Recently the use of transition metal oxysalts for these purposes was essayed and notorious performances were found in some cases, such as Mn carbonate[17] or Fe[18] and Co[19] oxalates, and metal formates.[20] Particularly, monodispersed forms of manganese carbonate with a calcite structure prepared by using reverse micelles were found to store reversibly lithium by a different mechanism than binary manganese oxides. The low molecular weight of the carbonate material allowed large electrode capacities, while the environmental friendliness of the oxysalt was considered an added value. However, the cycling behavior should be improved for practical applications and an analysis of the mechanisms involved in lithium storage into transition metal carbonates, including conversion and/or capacitive processes deserve further analysis.

The aim of this work is to study the cycling properties of $MnCO_3$ and Co-substituted $MnCO_3$-based electrodes and to gain further knowledge on possible effects of metal substitution and lithium storage mechanisms in carbonate electrodes. For this purposes several solid solutions in the $Mn_{1-x}Co_xCO_3$ system are prepared for the first time by the reverse micelles method. In addition, new spectroscopic and magnetic measurements are discussed to gain a better understanding on the lithium storage mechanisms.

EXPERIMENTAL SECTION

Submicronic particles of $Mn_{1-x}Co_xCO_3$ ($0 \le x \le 0.3$) were synthesized by a reverse micelles method. Two microemulsions of water-in-isooctane were prepared by stirring, followed by ultrasonic treatment, and stabilized by CTAB (hexadecyl-trimetyl ammonium bromide) surfactant and hexanol cosurfactant. The proportions of the various constituents in these microemulsions are as follows: 16.76% of CTAB, 13.9% of hexanol, 59.29% of isooctane, and 10.05% of the aqueous phase. The aqueous phase in the reverse micelles of microemulsion (I) contained 0.3 M of a mixture of manganese(II) nitrate tetrahydrate and cobalt(II) nitrate hexahydrate in the desired proportions; meanwhile, reverse emulsion (II) contained 0.3 M of sodium hydrogen carbonate as the aqueous phase. The insoluble product was precipitated as a result of coalescence between the reverse micelles of both microemulsions which were mixed, followed by ultrasound and stirred over the night on magnetic stirrer. The precipitate was separated from the solvent and surfactant by

Received: October 18, 2011
Published: May 8, 2012

dx.doi.org/10.1021/ic3004382 | Inorg. Chem. 2012, 51, 5554−5560

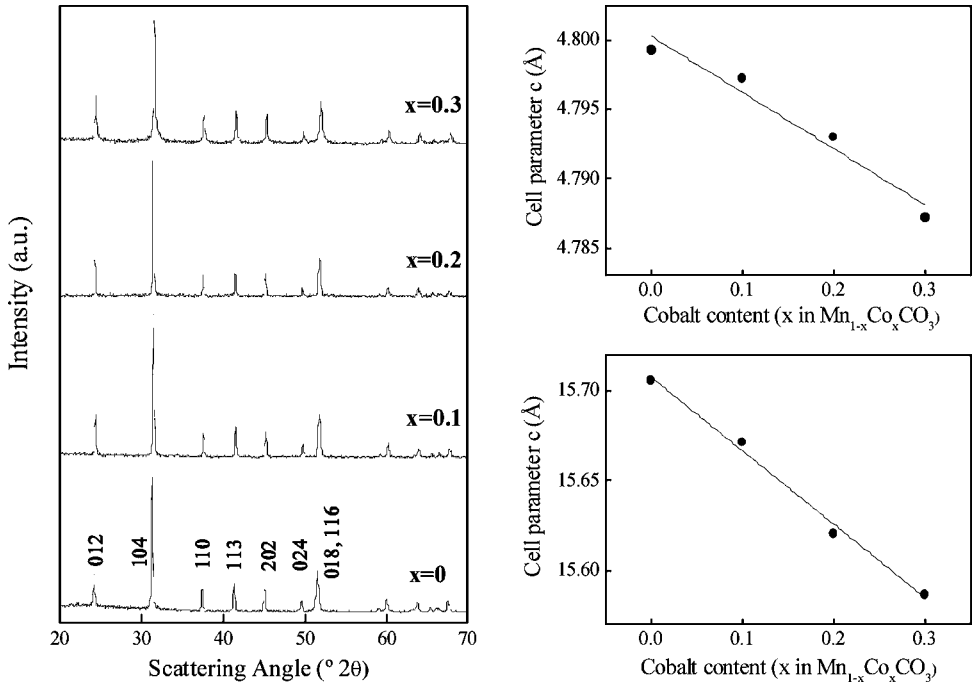

Figure 1. (left) X-ray pattern for $Mn_{1-x}Co_xCO_3$ samples ($0 \leq x \leq 0.3$). (right) Unit cell parameters variation as a function of the cobalt content.

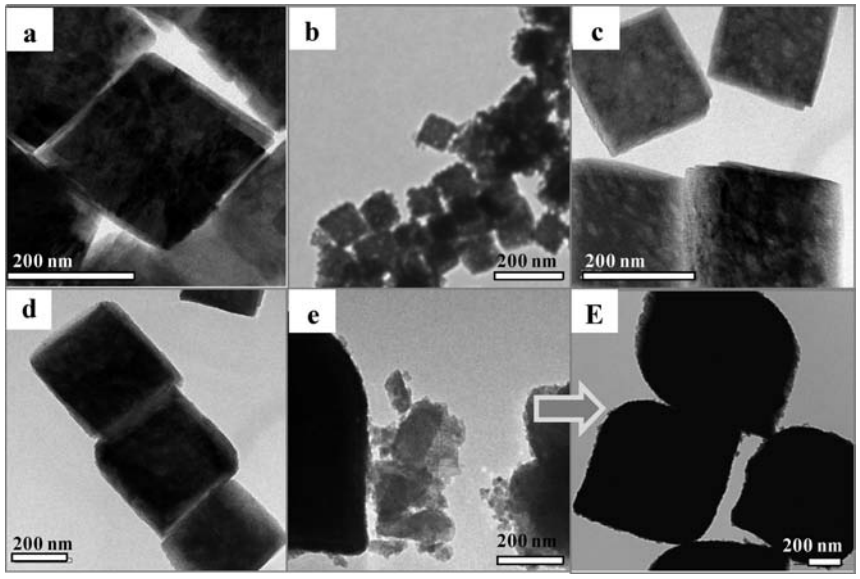

Figure 2. TEM images of the samples $Mn_{1-x}Co_xCO_3$ with $x = 0$ prepared with AOT (a), $x = 0$ prepared with CTAB (b), $x = 0.1$ (c), $x = 0.2$ (d), $x = 0.3$ (e, E).

centrifugation, rinsed with a 1:1 mixture of methanol and chloroform and dried at 80 °C under vacuum in a Buchi glass oven. Samples were heated under vacuum to temperatures before their decomposition temperatures.

X-ray diffraction (XRD) patterns were recorded on a Siemens D5000, using a graphite monochromator and Cu Kα radiation. The Rietveld analysis was carried out by using the FULLPROF software. Transmission electron microscopy (TEM) images in high and low resolution were obtained in JEOL 200CX and Philips CM-10 microscopes, respectively. Each sample was dispersed in a small amount in acetone and dropped on a copper grid for TEM examination. Thermogravimetric analysis (TGA) and differential thermal analysis (DTA) curves were obtained in a Shimadzu DTG-60AH instrument under air and argon atmospheres.

The EPR spectra in the X-band (9.23 GHz) were recorded as a first derivative of the absorption signal of an ERS-220/Q spectrometer within the temperature range of 90−400 K. To obtain the ex-situ EPR spectra of the electrochemically charged and discharged compositions, the electrochemical process was interrupted at selected charge levels. After several current pulses followed by voltage relaxation periods to reach the equilibrium voltage conditions, the electrochemical cells were dismantled in an Ar-containing drybox and the retrieved electrodes were used for the EPR measurements.

Magnetic measurements were carried out in a superconducting quantum interference device magnetometer (Quantum Design, model MPMS-XL). The temperature dependence of magnetization was measured upon heating samples from 2 to 300 K under zero-field cooled conditions. An applied magnetic field of 0.1 T was used.

dx.doi.org/10.1021/ic3004382 | Inorg. Chem. 2012, 51, 5554−5560

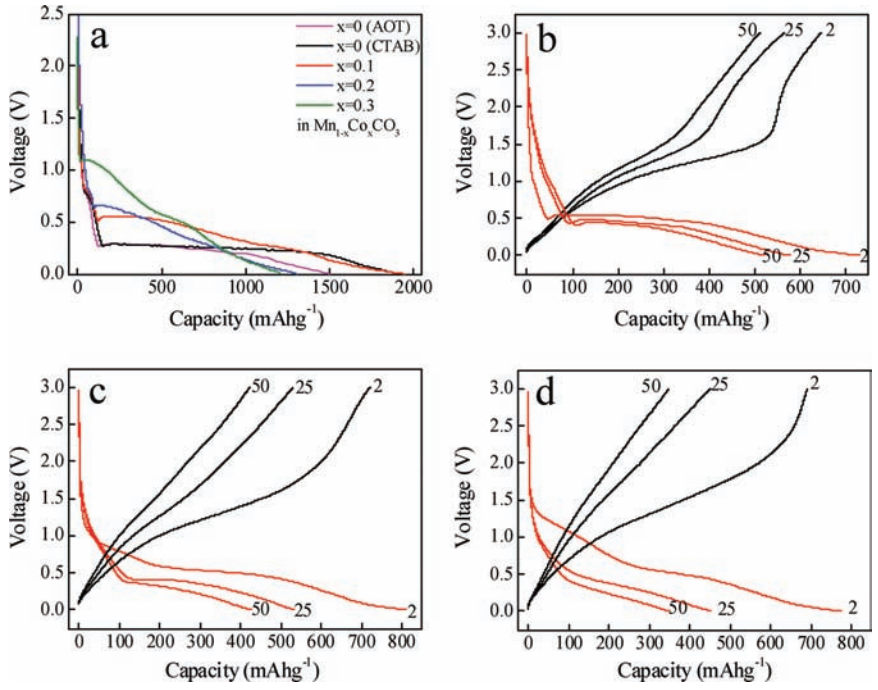

Figure 3. Galvanostatic results of lithium test cells: First discharge plots at C/5 rate (a), and selected cycles at C rate for $Mn_{1-x}Co_xCO_3$ prepared with CTAB with x = 0 (b), 0.1 (c), and 0.3 (d).

For the electrochemical studies, two-electrode Swagelok-type lithium cells were used. The slurry for the electrode was prepared by mixing the powdered active material (60%) with carbon black (30%) and polyvinylidene fluoride (10%) dissolved in N-methyl-pyrrolidone and dried at 120 °C. The slurry was deposited on a Cu foil, and the electrode was dried at 120 °C and under vacuum in a Buchi glass oven. The assemblage of the cells was done in an MBraun glovebox under argon atmosphere with H_2O/O_2 < 1 ppm. The prepared electrodes were used as cathode and lithium foils as anode. A mixture of ethylene carbonate and diethyl carbonate (EC:DEC) in a 1:1 weight proportion including 1 M $LiPF_6$ was used as electrolyte, and two Whatman glass microfiber papers were used as separator. Galvanostatic characterizations were carried out using C/5 rate (C = 1 Li h^{-1} mol^{-1}) charge/discharge cycles in VMP and Arbin multichannel microprocessor controlled systems. A blank experiment with only carbon showed a possible contribution of ca. 10% to the total capacity. Potentiostatic tests were performed at different sweep rates using a multichannel microprocessor controlled system, Macpille II.

RESULTS AND DISCUSSION

The XRD patterns of $Mn_{1-x}Co_xCO_3$ samples are collected in Figure 1 (left). All the samples show patterns in agreement with a calcite structure (rhombohedral lattice, $R\bar{3}c$ space group).[21,22] Co_3O_4 and CoO impurities were observed for x > 0.3 (samples not shown). Additionally a shift of the most intense reflection on increasing cobalt content was observed (Supporting Information Figure SI-1). The Rietveld analysis (Supporting Information Figure SI-2 and Table SI-1) agreed with the partial random substitution of Mn^{2+} by Co^{2+} ions in the calcite structure of the partially substituted carbonates. The evolution of unit cell parameters a and c versus cobalt content is fairly linear (Figure 1, right), which is in agreement with Vegard's law,[23] and is evidence that all the samples are solid solutions.

Figure 2 shows the TEM images of the samples, which consist of monodispersed regular particles for $Mn_{1-x}Co_xCO_3$ with x = 0, 0.1, and 0.2 with submicrometric particle size. The smaller size observed for $MnCO_3$ obtained under the same experimental conditions as substituted samples prompted us to prepare the same material by using Aerosol OT (AOT) surfactant (Figure 2a and b). This method leads to particles with similar size than $Mn_{1-x}Co_xCO_3$ with x = 0.1 and 0.2 (Figure 2c and d). The sample with x = 0.3 shows distorted/rounded regular agglomerates ("lemon" like) with submicrometric heterogeneous distribution of particle size, probably indicating the vicinity to the solubility limit of cobalt. The application of the Williamson–Hall method[24] to these patterns (Supporting Information Figure SI-3) showed that the differences in the size of the coherently diffracting domains were limited in these samples. The measured sizes were 185, 177, 389, and 224 nm for x = 0 prepared with AOT, x = 0.1, 0.2, and 0.3, respectively. The EDX measurements for all the samples (not shown) proved the homogeneous distribution of Co and Mn in different regions studied in each sample.

The TG curve for $MnCO_3$ under static air and dynamic argon was recorded (Supporting Information Figure SI-4). Under dynamic argon, the decomposition takes place at 300 °C according to eq 1:

$$MnCO_3 \rightarrow MnO + CO_2\uparrow \quad (1)$$

Concerning the variation of decomposition temperature with cobalt content, there was an increase from 305 to 335 °C on increasing cobalt content. All the samples were heated to temperatures below their decomposition in order to eliminate any residual water prior to electrochemical experiments.

Figure 3a shows the first discharge curves of lithium test cells recorded at C/5 rate for both $MnCO_3$ samples and for $Mn_{1-x}Co_xCO_3$ with x = 0.1, 0.2, and 0.3. The curves are characterized by a sharp voltage drop down to a voltage that depends on cobalt content, being ca. 0.3, 0.3, 0.5, 0.7, and 1.1 V, respectively. Irrespective of particle size, the first discharge voltages of $Mn_{1-x}Co_xCO_3$ electrodes are higher on increasing x, in agreement with the different reduction potentials of Mn^{2+} and Co^{2+}, as it is well established for conversion oxides.[13,25] The small plateau at ca. 0.8 V is probably due to electrolyte

dx.doi.org/10.1021/ic3004382 | Inorg. Chem. 2012, 51, 5554–5560

decomposition and SEI formation. Then, the curves follow a smoother decrease of the voltage down to 0 V, reaching capacity values between 1200 and 1900 mAh g^{-1}. By comparing the two $MnCO_3$ samples, it is clear that the maximum capacity is reduced by increasing particle size. The noticeable textural modification on the particles upon cobalt doping when using the same surfactant can be responsible to an important extent for electrochemical discrepancies instead of a certain role hold by cobalt. A list of materials (e.g., CuO, CoO, Co_3O_4, Fe_2O_3, ...) that sustain a conversion reaction with lithium undergo important modification of capacity and capacity fade upon cycling with changing the initial particle size.[13,25,26] By comparing AOT-$MnCO_3$ with $Mn_{0.9}Co_{0.1}CO_3$, which have similar particle size, it is clear that capacity increases significantly by a small addition of cobalt. However for larger contents, capacity decreases again.

Figure 3b–d shows selected charge/discharge curves of lithium test cells recorded at C rate for $Mn_{1-x}Co_xCO_3$ with x = 0, 0.1, and 0.3. Again, the voltage of the main effect increases upon cobalt addition. In the first charge, the voltage increases continuously up to 3.0 V, without the presence of any plateau. The difference between the capacity of first charge and discharge leads to a large irreversible capacity. However, the Coulombic efficiency is higher on further cycling: up to 75% from cycle 2–50. For $Mn_{0.7}Co_{0.3}CO_3$ electrodes, the charge voltages are higher, again in agreement with the different oxidation potentials of Mn^{2+} and Co^{2+}. Also, capacity fading is more enhanced, especially after the first ten cycles. Intermediate results were obtained for the other samples.

The observed capacity values are clearly higher than those expected for a simple conversion mechanism according to eq 2:

$$MCO_3 + 2Li^+ + 2e^- \rightarrow M + Li_2CO_3 \quad (2)$$

with a theoretical capacity of ca. 460 mAh g^{-1}.

In order to confirm that reaction 2 occurred, FTIR spectra were recorded (Figure 4). The difficulty in interpretation of these spectra comes from the possible contribution of the electrolyte solvent, as well as $(CH_2OCO_2Li)_2$ and Li_2CO_3 products coming from the electrolyte solvent decomposition.[27] Nevertheless, the presence of a band located at 1470–1480 cm^{-1} is consistent with the presence of $MnCO_3$ in both the original and cycled material. The spectra of both washed with cyclohexane and unwashed products showed this band. Having in mind that carbonate could form as a result of the electrolyte solvent decomposition some uncertainty could still be present if the washing process was incomplete. Further evidence on reaction 2 will be discussed below in the light of EPR and magnetic measurements.

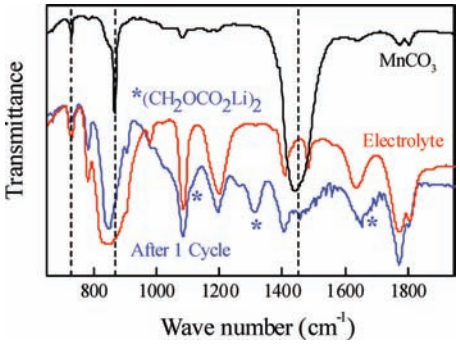

Figure 4. FTIR spectra of pristine $MnCO_3$ prepared with CTAB, electrolyte, and electrode after first cycle at C rate.

Figure 5 compares the cycling performance at C and 5C rates for selected compositions. As expected, the reversible capacities decrease on increasing the C rate. $MnCO_3$ retains capacities around 500 mAh g^{-1} after 80 cycles when cycled at C rate, while this value decreases to less than 300 mAh g^{-1} at 5C, values below the practical capacity of graphite. For x = 0.1 and 0.3, there is a progressive decrease in capacity for C rate. In contrast, Co-containing samples display better capacity retention upon cycling at 5C rate.

The potentiostatic charge/discharge second cycles for the samples of $Mn_{1-x}Co_xCO_3$ at a voltage sweep rate of 2 mV s^{-1} are presented in Figure 6 (left). Both the reduction and oxidation peaks assigned to Mn^{2+}/Mn and Co^{2+}/Co pairs increase their voltage on increasing cobalt content, again in agreement with the different reduction potentials,[13,25] and according to a conversion reaction of carbonates with lithium, as shown in eq 2.

In order to find out about the source of the extra high capacity in comparison with the theoretical capacity value related to the pure conversion reaction (eq 2), the faradic and capacitive contribution to the whole capacity were studied, according to the method developed by Dunn and co-workers.[28] The method used in the study is based on the fact that current is proportional to the square root of the scan rate for a diffusion-controlled system while a linear proportionality is expected for capacitive currents. Even for the multiphase mechanism of conversion reactions, diffusion can describe the kinetics well, if the motion of the interfaces is not rate-determining. According to ref 28, the total stored charge can be separated into two components: (1) the faradic contribution from the conversion reaction with lithium and (2) a complex contribution containing the faradic contribution from surface intercalation (pseudocapacitive contribution), together with the contribution from the double-layer effect (pure capacitive contribution). However, the reactions studied for the carbonates are not intercalation but conversion reactions, and thus the pseudocapacitive contribution coming from surface insertion/intercalation was assumed to be negligible. The result is presented in Figure 6 (right) as relative faradic contribution to the total capacity at different cobalt contents and different sweep rates. According to the figure, at low rates of discharge, the main component is the faradic contribution (ca. 80%) which decreases with increasing the sweep rate (Figure 6, right, upper scale). Part of this extra-capacity is then ascribable to reversible electrolyte degradation, as suggested by Tarascon et al.[13] On the other hand, increasing sweep rate from 0.5 to 20 mV s^{-1} leads to polarization enhancement, which results directly into the growth of capacitive contribution to the total capacity from 20% to 40%.

The faradic contribution increases with the cobalt content (Figure 6, right, lower scale) indicating that the reaction with lithium is favored for the higher amounts of cobalt. In fact, as the manganese content increases, the capacitive contribution (i.e., double layer effect) increases.

In order to confirm the role of manganese and the validity of reaction 2, EPR and magnetic susceptibility measurements were carried out on pristine $MnCO_3$ and used electrodes. $MnCO_3$ is a weak ferromagnet,[29] although antiferromagnetically ordered below its Néel temperature, ca. 34.5 K.[30,31] On the other hand, bulk α-Mn is an antiferromagnetic with a Néel temperature of

dx.doi.org/10.1021/ic3004382 | Inorg. Chem. 2012, 51, 5554–5560

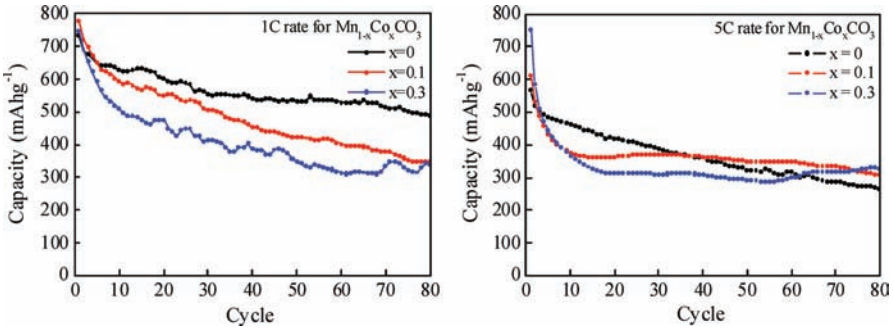

Figure 5. Capacity vs cycle number for $Mn_{1-x}Co_xCO_3$ prepared with CTAB with x = 0, 0.1, and 0.3 at C rate (left) and 5C rate (right).

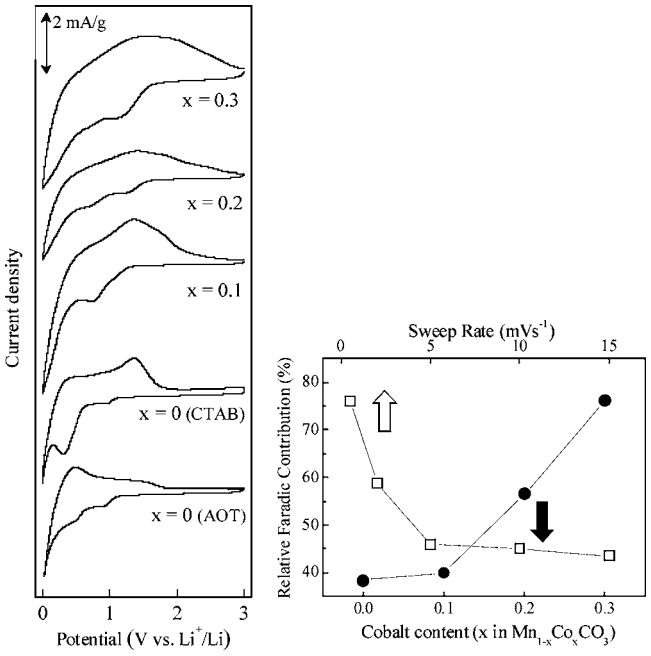

Figure 6. (left) Cyclic voltammetry for the samples of $Mn_{1-x}Co_xCO_3$ prepared with CTAB with x = 0, 0.1, 0.2, and 0.3, at 2 mV s^{-1}. (right) Relative contribution of faradic capacity to the total capacity for $Mn_{0.7}Co_{0.3}CO_3$ at different sweep rates (hollow squares), and at a scan rate of 0.5 mV s^{-1} versus cobalt content for the samples of $Mn_{1-x}Co_xCO_3$ (x = 0, 0.1, 0.2, and 0.3) (solid circles).

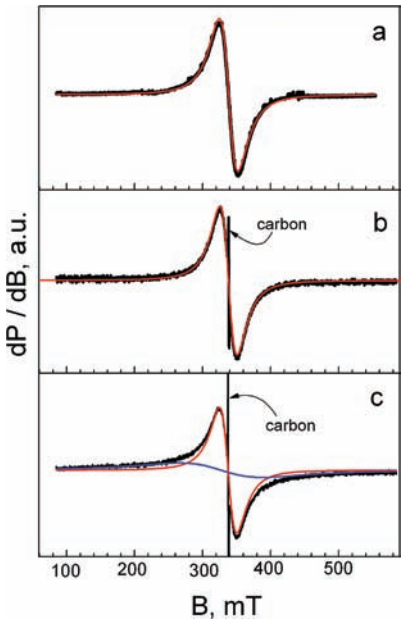

Figure 7. EPR spectra of pristine $MnCO_3$ prepared with CTAB and $MnCO_3$ electrode after the cell discharge to 0 V (b) and after the cell recharge to 3 V (c). The spectra are recorded at 293 K. The black, red, and blue lines correspond to the experimental spectra, simulated Lorentzian line due to Mn^{2+} in $MnCO_3$ and simulated Lorentzian line due to slightly exchange coupled Mn^{2+} ions.

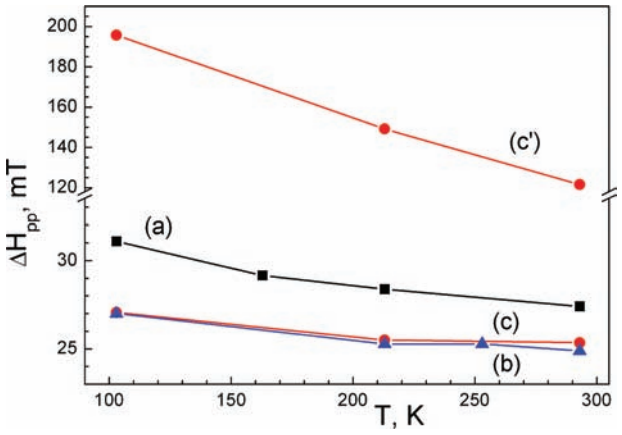

Figure 8. Temperature dependence of the EPR line width (ΔH_{pp}) of signals due to Mn^{2+} in $MnCO_3$ and slightly exchange coupled Mn^{2+} ions. The sample notation is as Figure 7.

95 K.[32] Thus these methods may provide valuable information on the electrochemical process.

The EPR spectrum of pristine $MnCO_3$ sample (Figure 7a) shows a single Lorentzian line with a g-factor value of 2.002. The signal broadens on decreasing the recording temperature until 100 K (Figure 7b). In the same temperature range, the signal intensity obeys the Curie–Weiss law with a Weiss constant of −57 ± 4 K. The EPR parameters are consistent with the magnetic structure of $MnCO_3$,[30,31] and the EPR signal is ascribable to antiferromagnetically coupled Mn^{2+} ions. After the electrochemical reaction with lithium, the EPR line width decreases slightly, while the same temperature dependence of the EPR line width is observed (see Figure 8). However, the EPR signal intensity is twenty five times lower than the intensity of pristine sample. Between 100 and 300 K, the signal intensity now follows the Curie–Weiss law with a Weiss constant of −48 ± 6 K. The narrower EPR signal of the electrode can be ascribed to traces of unreacted $MnCO_3$. The line width can be related with the particle size dimensions. The proposed formation of diamagnetic lithium salt (most probably lithium carbonate) diminishes the magnetic interactions between the nanoparticles of the unreacted $MnCO_3$. In

dx.doi.org/10.1021/ic3004382 | Inorg. Chem. 2012, 51, 5554–5560

addition, the electrochemical reaction would lead to reduction of Mn^{2+} to Mn^0, both having an electronic configuration with a zero angular orbital momentum, thus displaying close *g*-values. Above the Néel temperature, the EPR spectrum of α-Mn consists of a single Dysonian line with a line width decreasing with increasing of recording temperature. At 300 K, the EPR line width of α-Mn is about 30 mT.[33] Hence, bulk α-Mn does not contribute to the Lorentzian signal of electrodes. The lack of any EPR signal of Mn^0 can be related with manganese nanostructures, which according to ref 34 display complex magnetic properties.

The EPR spectrum of the electrode after Li extraction (Figure 7c) is close to that of the electrode discharged to 0 V: g = 2.00, line width of 25.3(3) mT and Weiss constant of -50 ± 5 K. In addition, a new signal with g-value of 2.01 becomes visible. This signal is broader in comparison with the signal from Mn^{2+} in crystalline $MnCO_3$: 120 vs 27 mT, respectively. On cooling, there is a line broadening. The signal intensity obeys the Currie–Weiss law with Weiss constant of -4 ± 5K. These EPR parameters correspond to Mn^{2+} ions that are slightly exchange coupled. This result clearly demonstrates that the oxidation state of the manganese ions is changed during the electrochemical reaction. In addition, the environment of the Mn^{2+} ions is also changed. It should be noted that MnO is an antiferromagnetic oxide with a Néel temperature of 120–125 K,[35] while Mn_3O_4 is ferrimagnetically ordered below the Curie temperature of 42 K.[36] Above the magnetic temperature, both MnO and Mn_3O_4 display EPR signals with *g*-value of 1.997–2.001 and 2.02–2.00, respectively.[37,38] The EPR line width varies with the composition and the particle size dimensions and changes between 40 and 500 mT.[35] In addition, manganese complexes with molecules from electrolytes (EC and/or DEC) can also contribute to the appearance of the broad EPR spectrum with *g*-value close to 2.00. Therefore, from EPR point of view, it is not possible to specify the environment of the slightly exchanged coupled Mn^{2+} ions. The significant change in Mn^{2+} environment can be interpreted by assuming that crystalline $MnCO_3$ with a calcite structure is not recovered after cell charge. However, it is unequivocally demonstrated that Mn^{2+} ions are recovered after removal of Li+ ions, and these ions can compensate their charge with carbonate ions in a non-X-ray-crystalline nanodispersed form.

On the other hand, SQUID measurements were carried out (Figure 9). For pure, submicronic $MnCO_3$, the effective magnetic moment at 298 K, 5.22 μ_B, is somewhat smaller than the expected value (5.92–6.10 μ_B) due to the particular antiferromagnetic interaction of Mn^{2+}. However, the measurements carried out on the mounted electrode showed a μ_{eff} = 4.10 μ_B, caused by the presence of carbon black and binder additives. Thus, in the following discussion, magnetic susceptibilities will be considered per gram of electrode. For the electrode after first discharge to 0 V, the data (Figure 9) are consistent with the loss of $MnCO_3$ and the presence of a paramagnetic contribution with no Curie–Weiss behavior. The magnetic susceptibility value (χ^{100K} = 1.402 × 10^{-5} emu g^{-1}) decreases significantly from the pristine electrode (χ^{100K} = 8.428 × 10^{-5} emu g^{-1}), which agrees with the loss of Mn^{2+} and the occurrence of Mn^0. However, manganese metal in its thermodynamically stable form below 1000 K, α-Mn, should display a broad maximum above the Néel temperature (95 K).[33] The absence of this effect can be attributed to nanometric Mn or Mn clusters.[34] Due to the ultrafine nature of the reaction products commonly found in conversion reactions,[13−20]

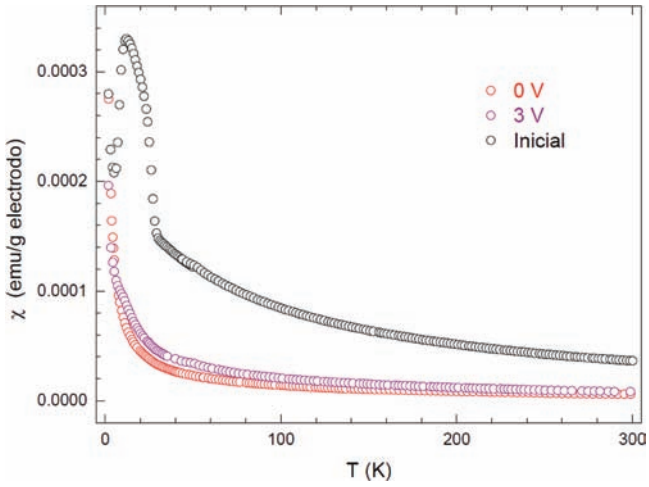

Figure 9. Magnetic susceptibility vs temperature for selected samples: (black circles) starting electrode prepared with CTAB; (red circles) 0 V; (magenta circles) 3 V.

crystalline manganese is not observed by XRD but annealing a simple in vacuum allowed to observe broad lines ascribable to α-Mn.[35]

After cell recharge to 3 V, crystalline $MnCO_3$ is not recovered (Figure, 9). However, Mn^{2+} seems to be partially recovered, as evidenced by the increase in the magnetic susceptibility to χ^{100K} = 2.042 × 10^{-5} emu g^{-1}. The weak signal at 55 K is due to the presence of oxygen in the system. These results support the previous interpretation of EPR data, by assuming that the Mn^{2+} ions which are recovered after cell charge compensate their charge with carbonate ions in a non-X-ray-crystalline nanodispersed form. In addition, the electrochemical results indicate that the Mn^{2+}/Mn pair is not the main contribution to the capacity of this electrode material, in agreement with the low faradaic and high capacitive contributions observed for Mn-rich compositions (Figure 6, right). In contrast, the enhanced activity of the Co^{2+}/Co pair was demonstrated for CoC_2O_4 by using XAS.[19]

CONCLUSIONS

A combined EPR-magnetic properties analysis of the electrochemical processes involving lithium storage into manganese carbonate reveals the reduction of Mn^{2+} ions to the metallic state, in a paramagnetic noncrystalline form. Manganese is partially reoxidized upon lithium extraction. Although the crystalline form of manganese carbonate is not recovered, carbonate ions can compensate the recovered Mn^{2+} ions in a noncrystalline product. The formation of submicrometric particles of $Mn_{1-x}Co_xCO_3$ solid solutions is reported. These solids store lithium by a conversion reaction together with a capacitive component. The presence of cobalt in low content enhances the cycling properties at higher rates as compared with the pure $MnCO_3$. This behavior could facilitate the selection of the best electrode according to each particular application.

ASSOCIATED CONTENT

Supporting Information

Figures SI.1–4 and Table SI.1 as mentioned in the text. This material is available free of charge via the Internet at http://pubs.acs.org.

dx.doi.org/10.1021/ic3004382 | *Inorg. Chem.* 2012, 51, 5554–5560

AUTHOR INFORMATION

Corresponding Author

*Tel.: +34957218637. E-mail: iq1ticoj@uco.es.

Notes

The authors declare no competing financial interest.

ACKNOWLEDGMENTS

The authors are indebted to MICINN (MAT2008-05880 and MAT2011-22753). S.M. is also grateful to EC for her Erasmus Mundus grant. R.S., M.Y., and E.Zh. are grateful to the financial support from the National Science Fund of Bulgaria (Ch1701/2007 and No DCVP-02/2/2009).

REFERENCES

(1) Mizushima, K.; Jones, P. C.; Wiseman, P. J.; Goodenough, J. B. *Mater. Res. Bull.* **1980**, *15*, 783.

(2) Dahn, J. R.; von Sacken, U.; Michal, C. A. *Solid State Ionics* **1990**, *44*, 87.

(3) Thackeray, M. M.; Johnson, P. J.; de Picciotto, L. A.; Bruce, P. G.; Goodenough, J. B. *Mater. Res. Bull.* **1984**, *19*, 179.

(4) Ohzuku, T.; Kitagawa, M.; Hirai, T. *J. Electrochem. Soc.* **1990**, *137*, 769.

(5) Alcántara, R.; Lavela, P.; Tirado, J. L.; Stoyanova, R.; Zhecheva, E. *J. Electrochem. Soc.* **1998**, *145*, 730.

(6) Alcántara, R.; Jaraba, M.; Lavela, P.; Tirado, J. L.; Biensan, Ph.; de Guibert, A.; Jordy, C.; Peres, J. P. *Chem. Mater.* **2003**, *15*, 2376.

(7) Padhi, A. K.; Nanjundaswamy, K. S.; Goodenough, J. B. *J. Electrochem. Soc.* **1997**, *144*, 1188.

(8) Lloris, J. M.; Pérez Vicente, C.; Tirado, J. L. *Electrochem. Solid-State Lett.* **2002**, *5*, A234.

(9) Nytén, A.; Abouimrane, A.; Armand, M.; Gustafsson, T.; Thomas, J. O. *Electrochem. Commun.* **2005**, *7*, 156.

(10) Dominko, R.; Bele, M.; Gaberscek, M.; Meden, A.; Remskar, M.; Jamnik, J. *Electrochem. Commun.* **2006**, *8*, 217.

(11) Manthiram, A.; Goodenough, J. B. *J. Electrochem. Soc.* **1989**, *26*, 403.

(12) Thackeray, M. M.; Baker, S. D.; Coetzer, J. *Mater. Res. Bull.* **1982**, *17*, 405.

(13) Poizot, P.; Laruelle, S.; Grugeon, S.; Dupont, L.; Tarascon, J. M. *Nature* **2000**, *407*, 496.

(14) Alcántara, R.; Jaraba, M.; Lavela, P.; Tirado, J. L. *J. Solid State Chem.* **2002**, *166*, 330.

(15) Chadwick, A. V.; Savin, S. L.; Fiddy, S.; Alcantara, R.; Lisbona, D. F.; Lavela, P.; Ortiz, G.; Tirado, J. L. *J. Phys. Chem. C* **2007**, *111*, 4636.

(16) Vidal-Abarca, C.; Lavela, P.; Tirado, J. L. *J. Phys. Chem. C* **2010**, *114*, 12828.

(17) Aragón, M. J.; Pérez-Vicente, C.; Tirado, J. L. *Electrochem. Commun.* **2007**, *9*, 1744.

(18) Aragón, M. J.; León, B.; Pérez Vicente, C.; Tirado, J. L. *Inorg. Chem.* **2008**, *47*, 10366.

(19) Aragón, M. J.; León, B.; Pérez Vicente, C.; Tirado, J. L.; Chadwick, A. V.; Berko, A.; Beh, S. Y. *Chem. Mater.* **2009**, *21*, 1834.

(20) Saravanan, K.; Nagarathinam, M.; Balaya, P.; Vittal, J. J. *J. Mater. Chem.* **2010**, *20*, 8329.

(21) Skinner, A. J.; Lafemina, J. P.; Jansen, H. J. F. *Am. Mineral.* **1994**, *79*, 205.

(22) Smyth, J. R.; Ahrens, T J. *Geophys. Res. Lett.* **1997**, *24*, 1595.

(23) Vegard, L. *Z. Phys.* **1921**, *5*, 17.

(24) Williamson, G. K.; Hall, W. H. *Acta Metal.* **1953**, *1*, 22.

(25) Zhong, K.; Xia, X.; Zhang, B.; Li, H.; Wang, Z.; Chen, L. *J. Power Sources* **2010**, *195*, 3300.

(26) Grugeon, S .; Laruelle, S.; Herrera-Urbina, R.; Dupont, L.; Poizot, P.; Tarascon, J. M. *J. Electrochem. Soc.* **2001**, *148*, A285.

(27) Aurbach, D.; Zaban, A.; Schechter, A.; Ein-Eli, Y.; Zinigrad, E.; Markovsky, B. *J. Electrochem. Soc.* **1995**, *142*, 2873.

(28) Brezesinki, T.; Wang, J.; Polleux, J.; Dunn, B.; Tolbert, S. H. *J. Am. Chem. Soc.* **2009**, *131*, 1802.

(29) Moriya, T. *Phys. Rev.* **1960**, *120*, 91.

(30) Robie, R. A.; Haselton, H. T., Jr.; Hemingway, B. S. *Am. Mineral.* **1984**, *69*, 349.

(31) Kosterov, A.; Frederichs, T.; von Dobeneck, T. *Phys. Earth Planet. Int.* **2006**, *154*, 234.

(32) Kohara, T.; Oda, Y.; Asayama, K. J. *Phys. Soc. Jpn.* **1975**, *38*, 1542.

(33) Lawson, A. C; Larson, A. C; Aronson, M. C.; Johnson, S.; Fisk, Z.; Canfield, P. C.; Thomson, J. D.; van Dreele, R. B *J. Appl. Phys.* **1994**, *76*, 7049.

(34) Zelený, M.; Šob, M.; Hafner, J. *Phys. Rev. B* **2009**, *80*, 144414.

(35) López-Ortega, A.; Tobia, D.; Winkler, E.; Golosovsky, I. V.; Salazar-Alvarez, G.; Estradé, S.; Estrader, M.; Sort, J.; González, M. A.; Suriñach, S.; Arbiol, J.; Peiró, F.; Zysler, R. D.; Dolors Baró, M.; Nogués, J. *J. Am. Chem. Soc.* **2010**, *132*, 9398.

(36) Boucher, B.; Buhl, R.; Perrin, M. *J. Appl. Phys.* **1971**, *42*, 1615.

(37) Golosovsky, I. V.; Arčon, D.; Jagličič, Z.; Cevc, P.; Sakhnenko, V. P.; Kurdyukov, D. A.; Kumzerov, Y. A. *Phys. Rev. B* **2005**, *72*, 144410.

(38) Winkler, E.; Zysler, R. D.; Fiorani, D. *Phys. Rev. B* **2004**, *70*, 174406.